

Feshbach resonances in cold collisions as a benchmark for state of the art *ab initio* theory

Karl P. Horn,¹ Meenu Upadhyay,² Baruch Margulis,³ Daniel M. Reich,¹ Edvardas Narevicius,^{4,5} Markus Meuwly,⁶ and Christiane P. Koch¹

¹*Dahlem Center for Complex Quantum Systems and Fachbereich Physik, Freie Universität Berlin, Arnimallee 14, 14195 Berlin, Germany*

²*Department of Chemistry, University of Basel, Basel, Switzerland.*

³*Department of Chemical and Biological Physics, Weizmann Institute of Science, 7610001 Rehovot, Israel.**

⁴*Department of Chemical and Biological Physics, Weizmann Institute of Science, 7610001 Rehovot, Israel*

⁵*Department of Physics, Technische Universität Dortmund, Dortmund, Germany*

⁶*Department of Chemistry, University of Basel, Basel, Switzerland*

(Dated: August 26, 2024)

Quantum resonances in collisions and reactions are a sensitive probe of the intermolecular forces. They may dominate the final quantum state distribution, as recently observed for Feshbach resonances in a cold collision experiment (Science 380, 77 (2023)). This raises the question whether the sensitivity of such measurements is sufficient to assess the quality of theoretical models for the interaction. We here compare measured collision cross sections to those obtained with exact quantum coupled-channels scattering calculations for three different *ab initio* potential energy surfaces. We find that the ability to test the correct prediction of energy redistribution over molecular degrees of freedom is within reach, requiring only a modest improvement in energy resolution of current experiments. Such improvement will enable the separation of individual resonances and allow for an unambiguous experimental test of different theory approaches.

Collisions probe the interaction between atoms and molecules, with experiments measuring the probability of the collision partners to change their state or undergo a chemical reaction¹. The comparison of measured and calculated collision cross sections allows us to quantify, in principle, how well our theoretical understanding matches physical reality in the experiments^{2,3}. In practice, however, such direct comparison of experimental data to theoretical predictions and thus quantitative assessment of theoretical models has long been hampered by the stringent requirement to properly resolve both initial and final states of a collision^{4,5}. This gap is being closed by cold and ultracold collisions which provide a means to prepare the initial state with sufficient energy resolution and quantum purity⁶. Final-state resolution has recently been added to these experiments by collecting the reaction products with velocity map imaging^{7–10}. Even with state-to-state resolution, it often is very challenging to identify measurable quantities with high sensitivity to the theoretical model¹¹. This is true in particular in collision systems where the interaction is strong enough to couple different internal and external degrees of freedom^{7,12–14}. The difficulty is to separate the contribution of quantum resonances from the direct collision process that usually proceeds via classical statistical dynamics⁷. Such a separation has been possible in electron-ion coincidence measurements of Penning ionization where the resonant dynamics in the collision of

the molecular ion with the neutral could be distinguished from the background contribution⁸. Here we show how a modest increase in energy resolution transforms the qualitative comparison between experimental results and theory into a quantitative one enabling an unequivocal confirmation or rejection of theoretical predictions at the highest level of state of the art *ab initio* theory. We confirm this by analyzing contributions of individual Feshbach resonance states to the final state distribution for three potential energy surfaces. Resolving such states is within experimental reach and will enable an unambiguous benchmark of the best *ab initio* models for strongly interacting systems.

Molecular collisions are typically well described within the Born-Oppenheimer approximation, which assumes an adiabatic separation of electronic and nuclear degrees of freedom. The interaction between the collision partners is then fully determined by the potential energy surface (PES). How much information about a PES can be inferred from measured cross sections depends, however, on characteristics such as the range and degree of anisotropy of the intermolecular interactions. For example, an almost fully statistical distribution over the energetically allowed final states was observed in reactive collisions with very strong anisotropy⁷, despite these collisions proceeding in the fully quantum regime with initial-state selection and at extremely low collision energies corresponding to a few hundreds nano-kelvin. In contrast, reactive collisions between rare gas atoms and dihydrogen molecules which are governed by an interaction with similarly strong anisotropy, revealed clear quantum fingerprints in their cross sections, thanks to the isolation of

* Current address: National Institute of Standards and Technologies, 80305 Boulder, CO, USA.

different reaction pathways⁸. For such a small collision complex, the numerical solution of the quantum scattering problem can be fully converged. The theoretical predictions for the cross section involve then only approximations that are made (on top of the Born-Oppenheimer approximation) when constructing the PES. These include primarily the level of quantum chemical theory and the accuracy with which the reference data can be represented. Changes in the shape of the PES should thus directly translate into modifications of the cross sections. One can then improve calculated potential energy surfaces, starting from the experimental data, through suitable coordinate transformations^{15–17}. Here instead, we revert this perspective and address the question by how much the experimental resolution of measured cross sections must improve in order to unambiguously discriminate predictions derived from different levels of advanced *ab initio* electronic structure theory.

We consider neon atoms interacting with dihydrogen molecular ions in the ($1^2A'$) electronic ground state. The electronic structure problem involves 11 electrons which is too large to be treated with full configuration interaction but amenable to the coupled-cluster method with single, double and perturbative triples excitations⁸ (the current "gold standard"¹⁸ of electronic structure theory) as well as multi-reference configuration interaction (MRCI) calculations^{19,20}, see Methods for more details on the PES. The dynamics on the ionic PES are initiated by Penning ionization²¹, which occurs upon collision of a metastable rare gas atom with a dihydrogen molecule^{22,23}. The ionization populates different vibrational states of the H_2^+ molecular ion which are resolved in the experiment thanks to measuring electrons and molecular ions in coincidence⁸. The cross sections then result from different, and independent, "initial" states⁸. Due to the pronounced anisotropy of the interaction, states with vibrational quantum number $v > 0$ may undergo rovibrational quenching — they are Feshbach resonances. The rovibrational quenching converts vibrational into rotational and kinetic energy. This is reflected in distinct peaks in the kinetic energy spectra⁸ which correspond to different final rotational states. The experimentally measured peak positions and heights agreed well with the results of full coupled-channel quantum scattering calculations using the CCSD(T) PES⁸, with the final state distributions clearly showing quantum fingerprints of the "initial" vibrational Feshbach resonances. At the same time, the calculated kinetic energy spectra contain finer details which disappear when convoluting the theoretical predictions with the finite energy resolution of the experiment⁸. In particular, and as we show below, details in the cross sections due to different shapes of the Feshbach resonances may get averaged out. This raises the question when the experimentally measured data will allow for discriminating theoretical predictions made with different PES.

In the following, we use three PESs obtained at the CCSD(T), resp. MRCI, levels of electronic structure the-

ory to determine the final state distributions from full coupled-channels quantum scattering calculations. Convoluting the predicted cross sections with the experimental energy resolution, we find that only a comparatively small increase in the latter will be sufficient to clearly distinguish theoretical predictions at different levels of advanced electronic structure theory. The three PESs differ in their long-range behavior and anisotropy, and comparing the different theoretical predictions allows us to identify how these are reflected in the kinetic energy spectra.

RESULTS

We consider "half-collisions" of neon atoms with dihydrogen molecular ions, launched by Penning ionization²¹ of a neutral dihydrogen molecule by a metastable neon atom. The ionization occurs at intermolecular separations of $\sim 9 a_0$ and can be modeled as a vertical transition to the electronic ground state of the molecular ion²⁴. It prepares weakly bound wavepackets, well approximated by a Gaussian function, with vibrational quantum numbers $v \geq 0$ and internal rotational quantum number $j = 0$ or $j = 1$ for para-, respectively ortho- H_2^+ ⁸. The total angular momentum J is conserved, as is parity, whereas the angular anisotropy of the interaction couples states with different v and j . This leads to rovibrational quenching whereby any change in j is accompanied by a change in the partial wave quantum number ℓ for the rotation around the center of mass of the collision complex, in order to preserve J (with $J \in \{|\ell - j|, \dots, \ell + j\}$). The remaining excitation energy is converted into kinetic energy of the molecular ion relative to the neon atoms. This energy can be measured by velocity map imaging²⁵. The corresponding spectra (as a function of the fragment kinetic energy) consist of a series of peaks that reflect the various possible final diatomic states. More precisely, each measured peak consists of contributions from different total angular momenta and partial waves⁸ which, unlike the final vibrational and rotational states, cannot easily be resolved in the experiment. Summing up these contributions implies some inevitable averaging over the quantum fingerprints of the collision dynamics. Despite the averaging, prior observations have shown that the final state distributions are linked to the intermolecular interactions⁸. It is thus reasonable to expect that the H_2^+ spectra display noticeable differences for different PESs as well.

The PESs that we have used in full-coupled channels quantum scattering calculations differ in the underlying approximations involved in the electronic structure methods (CCSD(T) vs MRCI), the basis sets used (aug-cc-pV5Z, indicated by the suffix '-5', and aug-cc-pVQZ, indicated by the suffix '-4' in the following), and their representations (parametrized fits vs. reproducing kernel Hilbert space). A comparison of the PESs^{8,19,20} is shown as supplemental material (SM)²⁶, with MRCI-

4 significantly deviating from CCSD(T)-5 and MRCI-5 in terms of minimal well-depth but also anisotropy. The electronic structure calculation method, spatial grid sampling, and interpolation including enforcement of the proper long-range behavior lead to smaller, but noticeable differences between the (single-reference) coupled cluster method and the two multireference methods.

Comparison of calculated and measured spectra

Figures 1 and 2 show the kinetic energy spectra obtained with the three PESs, for initial wavepackets with $v = 1$ and $v = 2$, convoluted with the experimental resolution, and shifted to minimize the root-mean-square (RMS) difference between computed and observed peak positions. Without adjustments, the peak positions can differ by up to 30 cm^{-1} . The peak positions indicate how much internal energy has been converted into kinetic energy and thus directly reflect the energy of the Feshbach resonances. Once this source of deviation between theoretical prediction and experimental data is accounted for, the remaining comparison, shown in Figs. 1 and 2(a)-(c), focusses on the distribution of the converted energy over the different final rovibrational states. The latter is mainly determined by the anisotropy of the interaction. Given the experimental resolution, all three PESs compare reasonably well with the experimental data. The broad peaks in Figs. 1 and 2(a)-(c), most of them well separated, correspond to the different *final* state contributions, characterised by the vibrational, internal rotational and partial wave quantum numbers v', j', ℓ' . In other words, it is almost always possible to resolve the final states when accounting for the experimental resolution⁸. In contrast, while without convolution most of the peaks in the kinetic energy spectra can be attributed to a specific *initial* state (with J, ℓ, j , shown in light shade), this information is lost after convolution. The bare, i.e., unconvoluted cross sections display much larger differences between the PESs. In some cases these differences are sufficiently large to remain visible even after convolution, most noticeably so for the peak around 600 cm^{-1} in Fig. 2 corresponding to the $v = 2, j = 1 \rightarrow v' = 1, j' = 7$ transition.

A more quantitative comparison needs to assess the agreement for both positions and heights of the peaks. In order to quantify the agreement for the peak positions, we introduce the energy $E_{\text{shift}}^{(\text{opt})}$ by which the spectra have to be shifted to optimally match the experimental peak positions. This shift has to be compared to the (velocity-dependent) experimental uncertainty in the peak positions which is about 20 cm^{-1} for the low- j' peaks but only 2 cm^{-1} for the high- j' peaks. The smallest shift by far is needed for the cross sections obtained with the CCSD(T)-5 PES, cf. Table I. To quantify the matching in terms of the peak heights, the (signed) differences $\chi^{(w)}$ are evaluated for an energy window w to assess the agreement on a per-peak basis. They are shown in

Figs. 1 and 2(d), confirming a similar performance of all three PES in terms of the peak heights, in particular for the strong peaks. Finally, a single figure of merit \mathcal{F} is obtained by averaging the RMS difference with respect to the energy shift up to the optimal value $E_{\text{shift}}^{(\text{opt})}$, see Methods. In terms of \mathcal{F} , the CCSD(T)-5 PES yields the closest match with the experimental data for both $v = 1$ and 2, cf. Table I. This is mainly due to the small energy shift $E_{\text{shift}}^{(\text{opt})}$ of less than 1 cm^{-1} . The advantage of the CCSD(T)-5 PES derives from the proper treatment of the long-range interaction which results in more accurate positions of the Feshbach resonances, as we show next.

Role of Feshbach resonances

Plotting the calculated cross sections as a function of the total collision energy, given as a sum of internal and kinetic energy, allows for a more in-depth analysis of the Feshbach resonances, cf. Fig. 3. Both the peak shapes and positions of the cross sections differ vastly between the PES. In particular, a clear bias towards lower energies is seen in the case of MRCI-5 and MRCI-4 as compared to CCSD(T)-5 for both $v = 1, 2$ and para- as well as ortho- H_2^+ . The higher resonance energies for CCSD(T)-5 are in line with the much smaller values of $E_{\text{shift}}^{(\text{opt})}$ as compared to MRCI-5 and MRCI-4. Moreover, the cross sections obtained with the MRCI-4 PES appear significantly broader than the other two. The para- H_2^+ cross sections for both $v = 1$ and $v = 2$ are primarily due to $\ell = 5, J = 5$ (shown with dark shade) and are comprised of three main peaks, corresponding to well-isolated Feshbach resonances. In contrast, for ortho- H_2^+ , where the dominant partial wave contribution consists of three different total angular momenta J , the cross sections indicate several, partially overlapping Feshbach resonances. Focusing specifically on $v = 1$ for para- H_2^+ , our analysis is facilitated by the fact that a single resonance, around $E = -17 \text{ cm}^{-1}$, dominates for CCSD(T)-5 whilst the cross sections obtained with MRCI-5 and MRCI-4 are both comprised of two significant contributions, occurring at lower energies, around -30 cm^{-1} and -70 cm^{-1} , respectively.

The cross section peaks in Fig. 3 are directly linked to the topology of the PES (shown as SM) and reflect the shapes of the resonance wavefunctions. At small inter-particle distances, the MRCI-4 PES differs from the CCSD(T)-5 and MRCI-5 ones, especially by its much more pronounced well-depth. The similar topologies of the CCSD(T)-5 and MRCI-5 PES at close range correspond with their peak intensities matching each other more closely than those obtained with the MRCI-4 PES. In contrast, at large inter-particle distances it is the CCSD(T)-5 PES that deviates strongly from its counterparts. Given the best performance of CCSD(T)-5 in terms of $E_{\text{shift}}^{(\text{opt})}$, this suggests the long range behaviour of

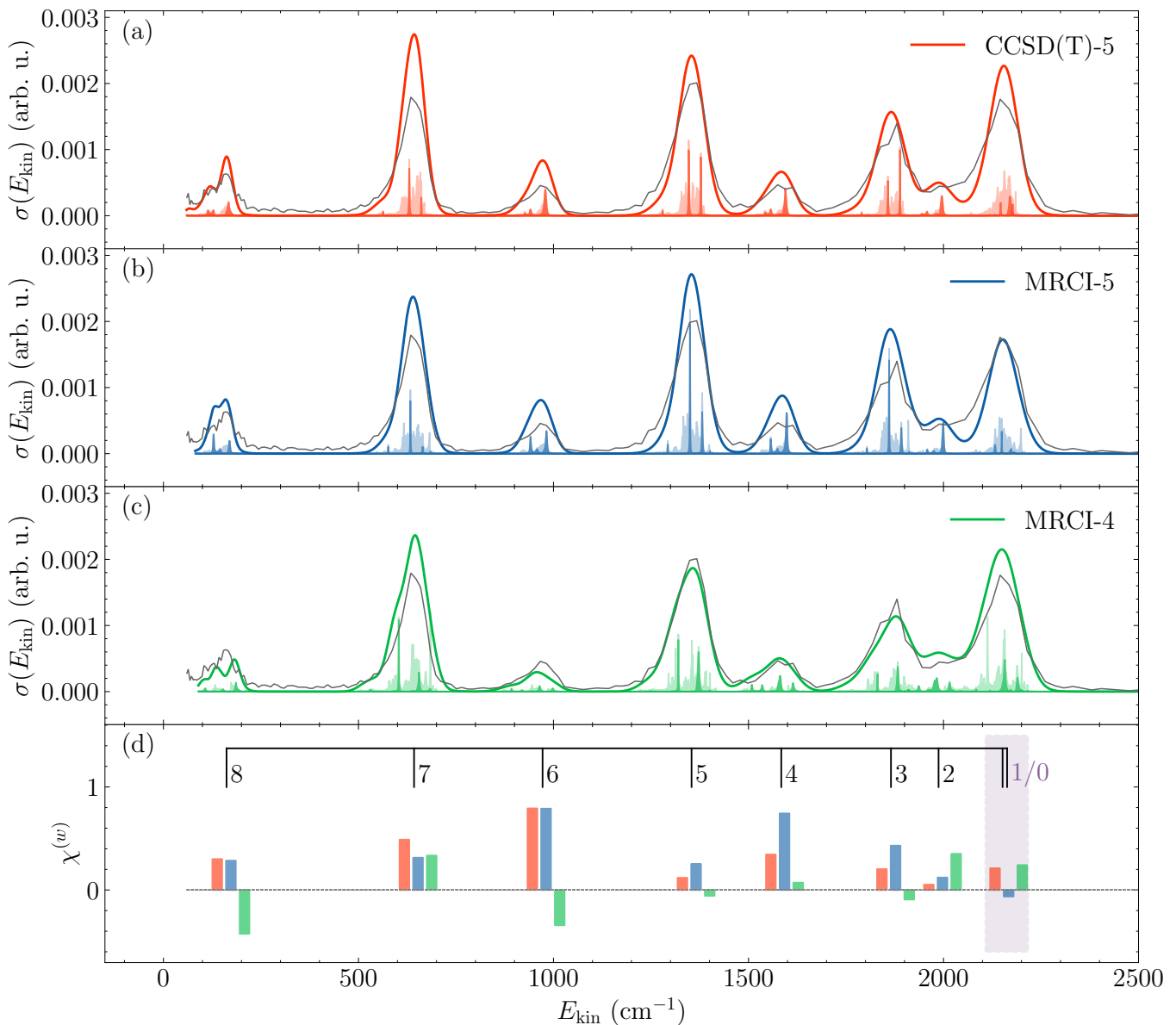


FIG. 1. Top three panels: Calculated cross sections (summed over all initial total angular momenta J and partial waves ℓ and product v', j', ℓ' and convoluted with the detector resolution) as a function of the kinetic energy, compared with the experimental data⁸ (grey) for an initial wavepacket with $v = 1, j = 0$. Each convoluted cross section is contrasted with its unconvoluted form (scaled to one tenth of its relative height compared to the convoluted cross section, lightly shaded areas). Darkly shaded areas indicate the dominant total angular momentum and partial wave combinations $\ell = 5$ and $J = 5$ for both para- and ortho- H_2^+ . Bottom panel: Integrated deviation of the theoretical predictions from the experiment $\Delta_{\text{opt}}^{(w)}$, as defined in Eq. (4), using the same colour coding as above. The window highlighted in purple is comprised of two final j' contributions as indicated by the comb.

the PES to be most relevant for the energies at which the Feshbach resonances occur and hence the peak positions. A close connection between the Feshbach resonance positions and the long-range part of the interaction had also been identified for half-collisions of helium, instead of neon, with H_2^+ molecules¹⁶. The conspicuously substantial anisotropy of the MRCI-4 PES and the resulting difference in cross sections indicate that the peak heights in the final v', j' -distribution are particularly sensitive to

the potential at short and intermediate R . This is where many avoided crossings between the adiabatic potential energy curves for each v, j (resulting from an adiabatic separation of vibrational and rotational motion) are observed⁸. Passage through the crossings redistributes the energy to the various final v', j' states which in turn is reflected in the peak height of the cross sections.

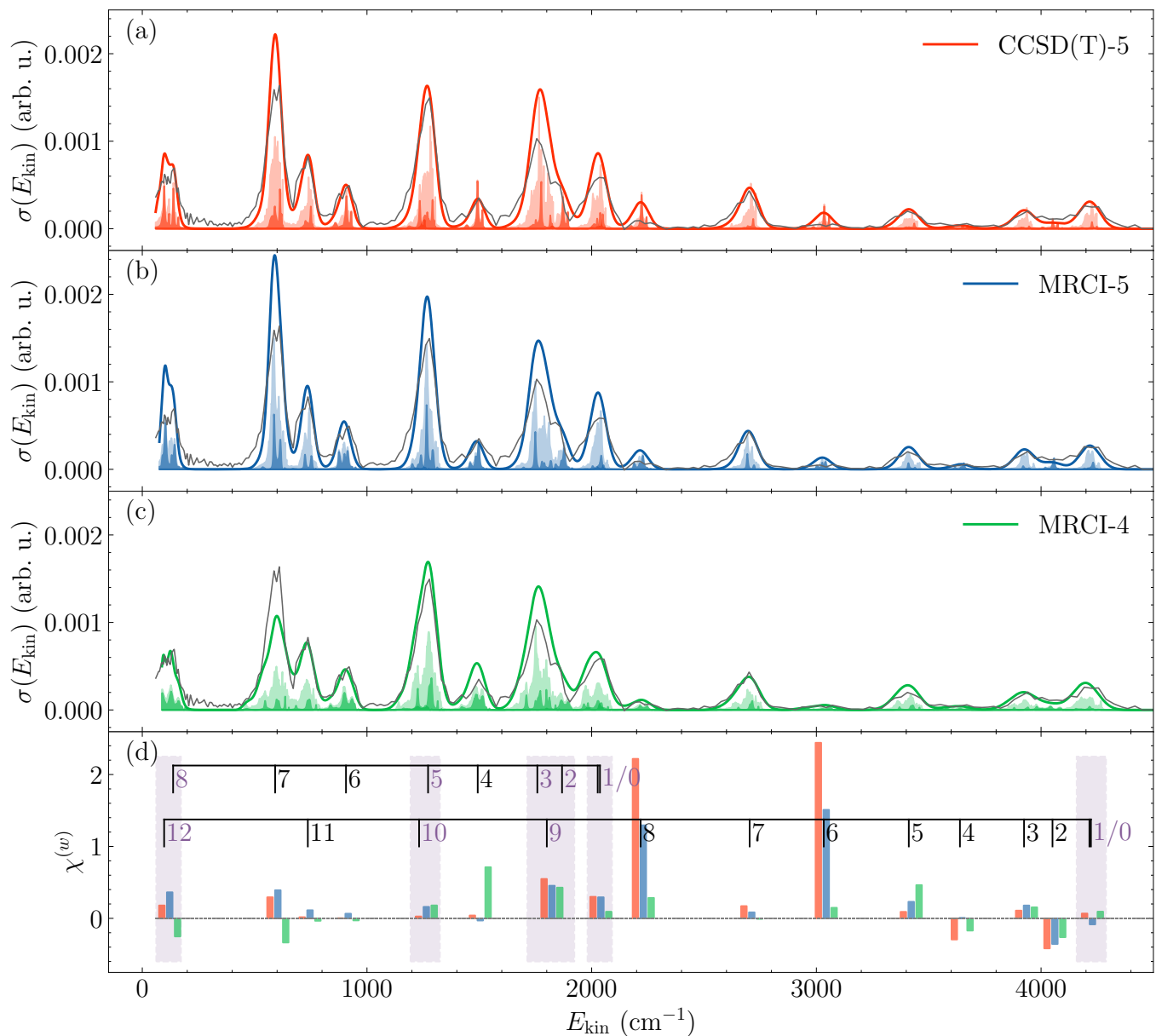


FIG. 2. Same as Fig. 1 but for the initial wavepacket with $v = 2, j = 0$. The unconvoluted cross sections have been scaled by a factor of three tenths relative to their convoluted counterparts.

v	PES	\mathcal{F}	$\min_{E_{\text{shift}}} \Delta(E_{\text{shift}})$	$\Delta(0)$	$E_{\text{shift}}^{(\text{opt})}$
1	CCSD(T)-5 ⁸	$9.9 \cdot 10^{-3}$	$9.9 \cdot 10^{-3}$	$9.9 \cdot 10^{-3}$	-0.74 cm^{-1}
	MRCI-5 ¹⁹	$1.2 \cdot 10^{-2}$	$1.0 \cdot 10^{-2}$	$1.6 \cdot 10^{-2}$	21.0 cm^{-1}
	MRCI-4 ²⁰	$1.1 \cdot 10^{-2}$	$7.9 \cdot 10^{-3}$	$1.6 \cdot 10^{-2}$	30.0 cm^{-1}
2	CCSD(T)-5	$8.5 \cdot 10^{-3}$	$8.5 \cdot 10^{-3}$	$8.5 \cdot 10^{-3}$	-0.54 cm^{-1}
	MRCI-5	$1.1 \cdot 10^{-2}$	$9.7 \cdot 10^{-3}$	$1.2 \cdot 10^{-2}$	16.0 cm^{-1}
	MRCI-4	$9.0 \cdot 10^{-3}$	$7.3 \cdot 10^{-3}$	$1.2 \cdot 10^{-2}$	27.0 cm^{-1}

TABLE I. Quantifying the agreement between calculated and experimental cross sections in terms of the figure of merit \mathcal{F} , cf. Eq. (3); the RMS deviation obtained for the energy shifted spectrum $\min_{E_{\text{shift}}} \Delta(E_{\text{shift}})$, cf. Eq. (2); the RMS deviation for the unshifted spectrum $\Delta(0)$; and the optimal energy shift $E_{\text{shift}}^{(\text{opt})}$. Values are reported with normalisation according to Eq. (1). For both “initial” vibrational states, the PES that performs best for a given quantifier is highlighted, using the color code of Figs. 1 and 2.

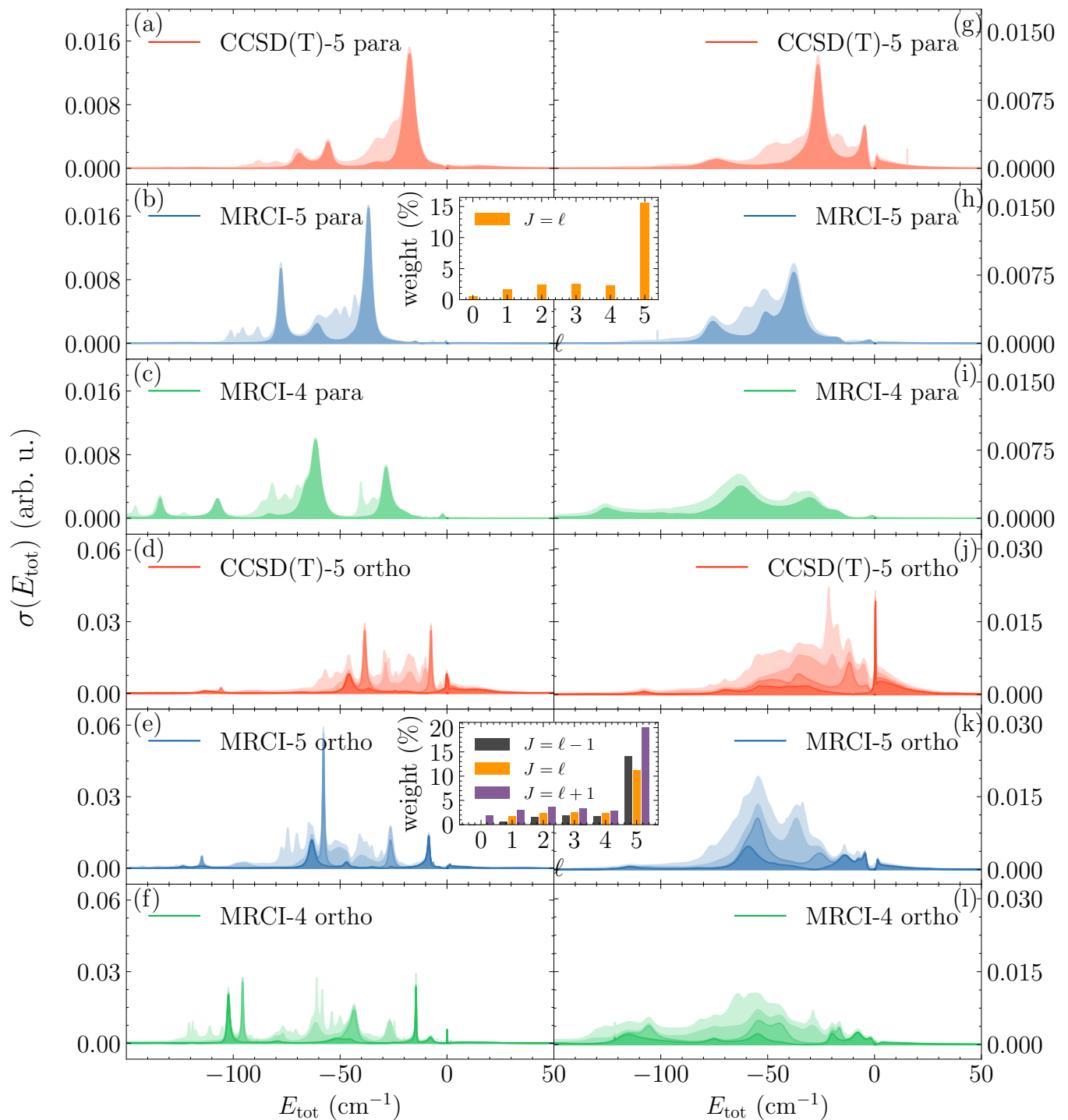


FIG. 3. Calculated collision cross sections as a function of the total energy. The left (right) panels correspond to initial diatomic vibrational states of $v = 1$ ($v = 2$). The three top (bottom) rows show the total cross section for para- H_2^+ with initial $j = 0$ (ortho- H_2^+ with initial $j = 1$) as a lightly shaded background and the specific contribution of the initial $\ell = 5$ partial wave and $J = 5$ as a darkly shaded slab ($J = 4, 5, 6$ from dark to light, bottom to top shaded slabs of cross section respectively). The insets indicate the individual weights of the various J, ℓ contributions.

Dependence on experimental resolution

Finally, we ask by how much the experimental resolution needs to be improved in order to clearly distinguish the predictions obtained with the three different PESs. To this end, kinetic energy spectra for three different experimental resolutions – the current one as well as a four-fold, resp. ten-fold improved resolution – are compared in Fig. 4. The decomposition of the unconvoluted cross section according to the total angular momentum J and initial partial waves ℓ (multiplied with -1 and offset for better visibility) is also shown in Fig. 4: Contributions with larger J and ℓ tend to occur at larger kinetic energies, most noticeably in the case of para- H_2^+ . When scaling the resolution, we take the convolution width to be independent of the kinetic energy whereas a kinetic energy-dependent convolution width accounts for experimental uncertainty⁸. For the sake of comparison, Fig. 4 shows the convoluted final state distribution at the present experimental resolution⁸ using the energy-dependent (dashed) and the fixed (brown solid lines) convolution widths, along with the curves for four-fold and ten-fold improved resolutions (with fixed widths). The differences between the fixed-width and energy-dependent convolution widths are only minor.

At the equivalent of four times the current experimental resolution, the first discernible splitting in peaks occurs. In this case, the convoluted spectra start to display a different energy dependence for the different PES, as opposed to just vary from each other in terms of overall peak heights. For the contribution of the dominant initial partial wave ($\ell = 5$) and in some cases also for the initial partial waves with lower weight, individual peaks in the spectra can be attributed to specific Feshbach resonances occurring at different energies, for example the peaks at kinetic energies of 175 cm^{-1} and 625 cm^{-1} . To emphasize this point, vertical purple lines in Fig. 4 indicate maxima of the cross section (solid lines) or minima of the second-derivative, i.e., shoulders (dashed lines). For example, in the case of CCSD(T)-5, the $\ell = 5$ contribution to the $j' = 8$ exit channel is comprised of three distinct peaks, seen at roughly 115 cm^{-1} , 130 cm^{-1} and 170 cm^{-1} in Fig. 4(a); they correspond to the three peaks at -70 cm^{-1} , -55 cm^{-1} and -20 cm^{-1} in Fig. 3(a). For MRCI-5, two pronounced peaks are seen at 130 cm^{-1} and 170 cm^{-1} and a flatter peak at roughly 140 cm^{-1} in Fig. 4(b), which can be attributed to the various peaks occurring at about -80 cm^{-1} , -60 cm^{-1} and -35 cm^{-1} in Fig. 3(b). MRCI-4, in contrast, displays broad peaks at around 110 cm^{-1} , 150 cm^{-1} and 185 cm^{-1} in Fig. 4, corresponding to the -110 cm^{-1} , -60 cm^{-1} and -30 cm^{-1} peaks in Fig. 3(c). To conclude, enhancing the energy resolution by a factor of four has a two-fold effect: On top of deciding which of the PES best captures the details of the interaction, it will also allow for assigning the peaks in the kinetic energy spectrum to specific Feshbach resonances.

At the equivalent of ten times the experimental resolu-

tion, the splitting is much more pronounced and several peaks can be clearly attributed to different initial J, ℓ channels. At the same time, there are also initial channels whose contributions cannot be resolved, for example at 650 cm^{-1} for the CCSD(T)-5 PES in Fig. 4(g), which corresponds to a total energy of -20 cm^{-1} in Fig. 3(d). Overall, however, and most importantly, the collision complex features sufficiently many, energetically well-isolated Feshbach resonances such that the shapes of the convoluted cross sections differ vastly amongst the three PES.

A direct comparison of the predictions obtained with the three different PESs is shown for two selected peaks at three different energy resolutions in Fig. 5(a-c) and (e-g). For both peaks, the largest gain in improving the ability to differentiate the PESs is observed when increasing the resolution by a factor of four. In order to make this observation more quantitative, Fig. 5(d,h) shows the peak-wise RMS deviation between pairs of simulated spectra (indicated by the color code) over the energy window shown in Fig. 5(a-c), respectively (e-g). A large increase in the RMS deviation corresponds to an increase in the ability to distinguish two theoretical predictions from each other, and thus also their respective comparison with the experimental data. As one would expect, increasing the resolution will not lead to an improved distinguishability indefinitely. At which resolution saturation sets in depends on the specific peak, i.e., the final j' values: While no substantial further improvement is observed in Fig. 5(d) when increasing the energy resolution by more than a factor of ten, in Fig. 5(h) the distinguishability continues to increase gradually even until 30 times the original resolution.

While a ten-fold increase in the kinetic energy resolution compared to the recent experiment⁸ may prove very challenging, a four-fold increase will require only moderate changes to the existing setup. With the corresponding kinetic energy resolution, it will already be possible to attribute a good part of the kinetic energy spectrum to specific initial *and* final states, taking the experiment a big step towards fully resolved ‘quantum tomography’ of the collision. This will come on top of the ability of the measurement to decide which level of theory for the interparticle interactions captures physical reality best.

METHODS

Full quantum coupled channels scattering calculations to obtain the cross sections have been performed as described earlier⁸. To compare cross sections with each other, the theoretical and experimental cross sections shown above have been ‘normalised’ according to

$$a \int_{\mathbb{R}_+} dE_{\text{kin}} \tilde{\sigma}_{\text{exp}}(E_{\text{kin}}) = b \int_{\mathbb{R}_+} dE_{\text{kin}} \tilde{\sigma}_{\text{theory}}(E_{\text{kin}}) = 1 \quad (1)$$

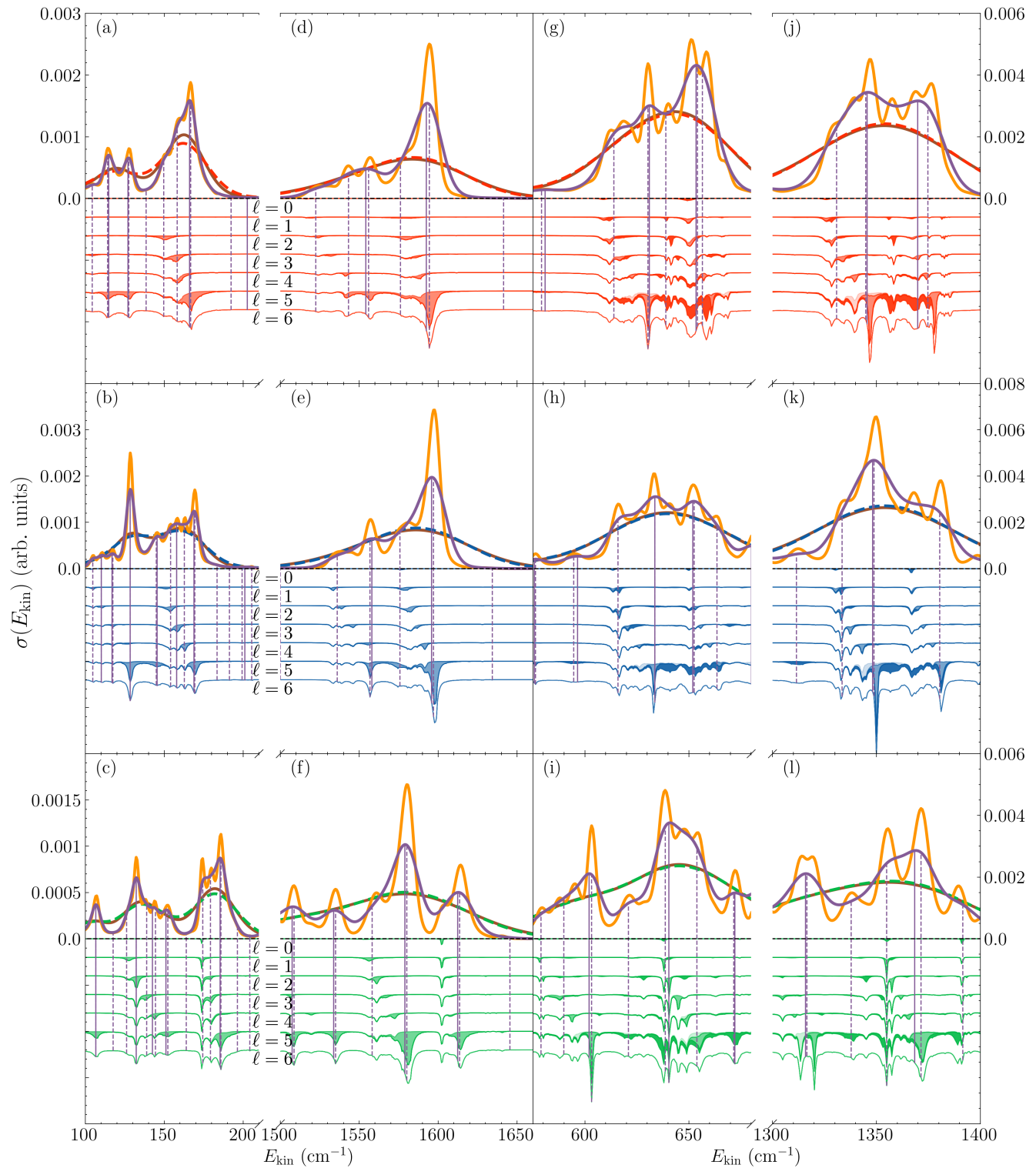


FIG. 4. Role of the convolution width in the calculated cross sections as a function of kinetic energy, starting from the current energy-dependent width⁸ (dashed lines with PES colour coding) and its approximation using a fixed convolution width (brown solid lines): Peaks which appear broad in Fig. 1 and are degenerate (in J, ℓ) start to show substructure when improving the (fixed-width) experimental resolution by a factor of four (purple), resp. 10 (gold). More pronounced differences between cross sections calculated with different PES then become visible. The energy windows shown for para(ortho)- H_2^+ (left and right column) correspond to the peaks with $j' = 8$ and $j' = 4$ ($j' = 7$ and $j' = 5$). Also shown are the individual contributions of the various initial channels, starting from $J, \ell = 0$, with light, intermediate, and dark shading corresponding to $J - \ell = -1, 0, 1$.

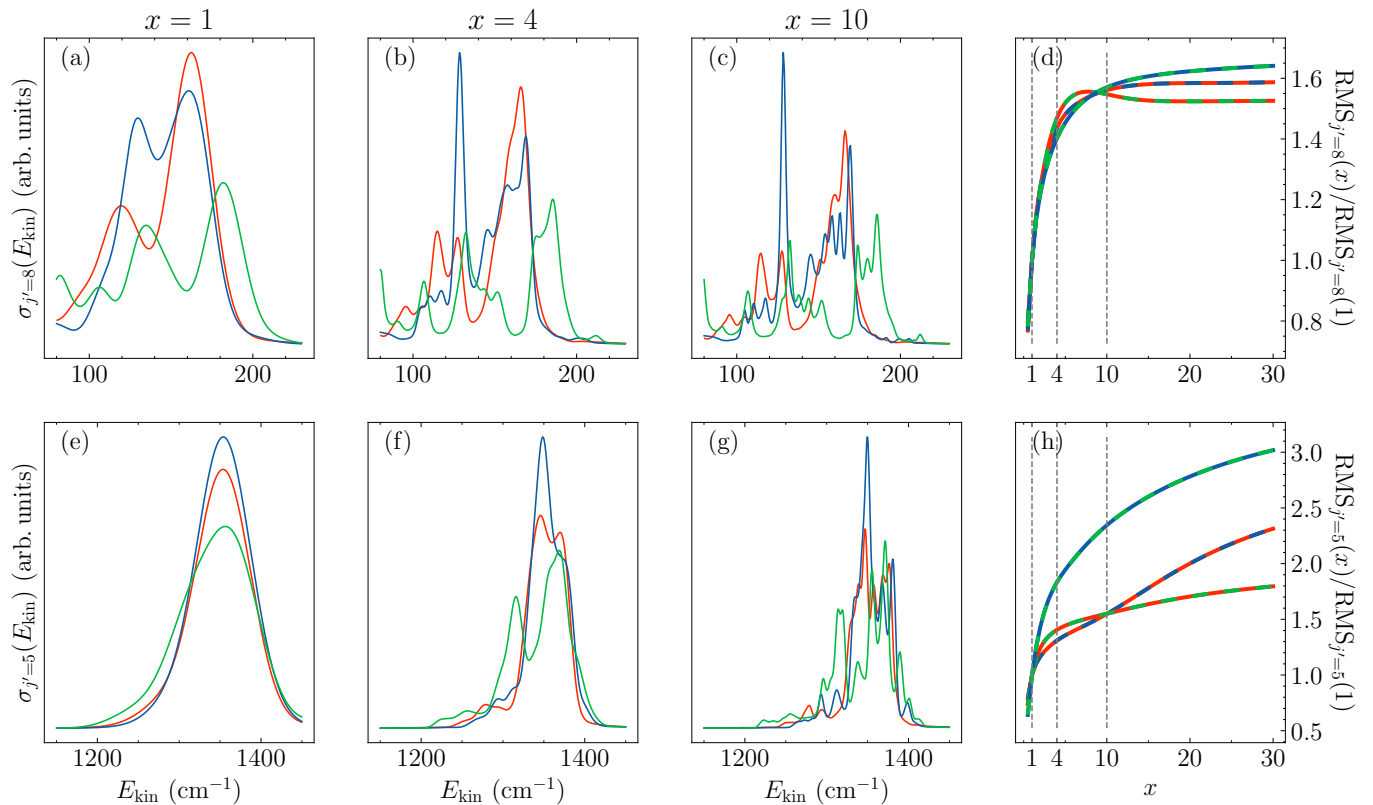


FIG. 5. Comparison of the cross sections as a function of kinetic energy, calculated with the three different PES, for increasing experimental resolution x and the peaks corresponding to $j' = 8$ (a-c) and $j' = 5$ (e-g). Panels (d,h) show the change in the RMS deviation for each pair of PES (as indicated by the color coding) as the resolution is enhanced.

for each potential energy surface. In Eq. (1), $\tilde{\sigma}_{\text{exp}}(E_{\text{kin}})$ and $\tilde{\sigma}_{\text{theory}}(E_{\text{kin}})$ are the cross sections prior to normalisation, whilst their rescaled counterparts appear without tildes. We discuss potential drawbacks of this scaling method and introduce an alternate method as supplemental material (SM). In particular, we show in the SM how this leads to a better overall agreement in terms of RMS deviation, but at the cost of an increase in the complexity.

When quantifying how well the calculated cross sections match the experimental cross section, we separate the mismatch in Feshbach resonance energies from the mismatch in the final state distribution, i.e., the amplitudes of the peaks corresponding to a given v' and j' . For each potential energy surface we find the most favourable E_{shift} by solving the minimization problem,

$$\begin{aligned} & \min_{E_{\text{shift}}} \Delta(E_{\text{shift}}) \\ & = \min_{E_{\text{shift}}} \sqrt{\int_{\mathbb{R}_+} dE_{\text{kin}} |\sigma_{\text{exp}}(E_{\text{kin}}) - \sigma_{E_{\text{shift}}}(E_{\text{kin}})|^2}, \end{aligned} \quad (2)$$

with

$$\sigma_{E_{\text{shift}}}(E_{\text{kin}}) = \sigma_{\text{theory}}(E_{\text{kin}} + E_{\text{shift}})$$

the energy shifted cross section, using the NLOpt python package²⁷. $\Delta(E_{\text{shift}})$ in Eq. (2), is the root-mean-square difference between the (energy-shifted) theoretical and experimental cross sections, which quantifies the error in the distribution of peak heights and shapes. We will refer to the optimal shift (in terms of the best match of peak positions) as $E_{\text{shift}}^{(\text{opt})}$.

Neither $\Delta(E_{\text{shift}} = 0)$, which emphasises the correctness of the Feshbach resonance energies over the correctness of peak amplitudes, nor $\Delta(E_{\text{shift}}^{(\text{opt})})$, which emphasises the correctness of the peak amplitudes over the peak positions, alone can fully characterize the agreement between calculated and experimental cross sections. For a fair comparison, we combine $E_{\text{shift}}^{(\text{opt})}$ and the root-mean-square deviation into a single figure of merit. To this end, we average $\Delta(E_{\text{shift}})$ over the interval $[\min(0, E_{\text{shift}}^{(\text{opt})}), \max(0, E_{\text{shift}}^{(\text{opt})})]$, i.e.,

$$\mathcal{F} = \frac{\int_0^{E_{\text{shift}}^{(\text{opt})}} dE_{\text{shift}} \Delta(E_{\text{shift}})}{\int_0^{E_{\text{shift}}^{(\text{opt})}} dE_{\text{shift}}}. \quad (3)$$

For a more fine-grained quantification of the differences, it is instructive to divide up kinetic energy histograms into windows $w = [w_{\text{min}}, w_{\text{max}}]$ corresponding to distinct peaks, with $\mathcal{W} = \{w\}$, the set of all windows. Unsigned integral deviations for matching theory and experiment on a per peak basis are given by⁸

$$\chi^{(w)} = \frac{\int_{w_{\text{min}}}^{w_{\text{max}}} dE_{\text{kin}} (\sigma_{E_{\text{shift}}}(E_{\text{kin}}) - \sigma_{\text{exp}}(E_{\text{kin}}))}{\int_{w_{\text{min}}}^{w_{\text{max}}} dE_{\text{kin}} \sigma_{\text{exp}}(E_{\text{kin}})}. \quad (4)$$

ACKNOWLEDGMENTS

We acknowledge financial support from the Swiss National Science Foundation (NCCR MUST, 200020_219779, 200021_215088) and the AFOSR (to MM).

-
- [1] R. E. Johnson, *Introduction to Atomic and Molecular Collisions* (Plenum Press, New York, 1982).
- [2] H. Friedrich, *Scattering Theory* (Springer Berlin, Heidelberg, 2013).
- [3] T. Karman, M. Tomza, and J. Pérez-Ríos, Ultracold chemistry as a testbed for few-body physics, *Nature Phys.* **20**, 722 (2023).
- [4] X. Yang, State-to-state dynamics of elementary bimolecular reactions, *Annual Review of Physical Chemistry* **58**, 433 (2007).
- [5] J. Jankunas and A. Osterwalder, Cold and controlled molecular beams: Production and applications, *Annual Review of Physical Chemistry* **66**, 241 (2015).
- [6] O. Dulieu and A. Osterwalder, *Cold Chemistry: Molecular Scattering and Reactivity Near Absolute Zero* (The Royal Society of Chemistry, 2017).
- [7] Y. Liu, M.-G. Hu, M. A. Nichols, D. Yang, D. Xie, H. Guo, and K.-K. Ni, Precision test of statistical dynamics with state-to-state ultracold chemistry, *Nature* **593**, 379 (2021).
- [8] B. Margulis, K. P. Horn, D. M. Reich, M. Upadhyay, N. Kahn, A. Christianen, A. van der Avoird, G. C. Groenenboom, M. Meuwly, C. P. Koch, and E. Narevicius, Tomography of Feshbach resonance states, *Science* **380**, 77 (2023).
- [9] G. Tang, M. Besemer, S. Kuijpers, G. C. Groenenboom, A. van der Avoird, T. Karman, and S. Y. T. van de Meerakker, Quantum state-resolved molecular dipolar collisions over four decades of energy, *Science* **379**, 1031 (2023).
- [10] V. Plomp, X.-D. Wang, J. Klos, P. J. Dagdigian, F. Lique, J. Onvlee, and S. Y. van de Meerakker, Imaging Resonance Effects in C + H₂ Collisions Using a Zeeman Decelerator, *The Journal of Physical Chemistry Letters* **15**, 4602 (2024).
- [11] M. Morita, R. V. Krems, and T. V. Tscherbul, Universal probability distributions of scattering observables in ultracold molecular collisions, *Phys. Rev. Lett.* **123**, 013401 (2019).
- [12] H. Zhou, W. Perreault, N. Mukherjee, and R. N. Zare, Anisotropic dynamics of resonant scattering between a pair of cold aligned diatoms, *Nature Chem.* **14**, 658 (2022).
- [13] T. de Jongh, Q. Shuai, G. L. Abma, S. Kuijpers, M. Besemer, A. van der Avoird, G. C. Groenenboom, and S. Y. T. van de Meerakker, Mapping partial wave dynamics in

scattering resonances by rotational de-excitation collisions, *Nature Chem.* **14**, 538 (2022).

- [14] M. P. Man, G. C. Groenenboom, and T. Karman, Symmetry breaking in sticky collisions between ultracold molecules, *Phys. Rev. Lett.* **129**, 243401 (2022).
- [15] M. Meuwly and J. M. Hutson, Morphing ab initio potentials: A systematic study of Ne-HF, *The Journal of Chemical Physics* **110**, 8338 (1999).
- [16] K. P. Horn, L. I. Vazquez-Salazar, C. P. Koch, and M. Meuwly, Improving potential energy surfaces using experimental Feshbach resonance tomography, *Science Adv.* **10**, eadi6462 (2024), 2309.16491.
- [17] J. M. Bowman and B. Gazdy, A simple method to adjust potential energy surfaces: Application to hco, *J. Comp. Phys.* **94**, 816 (1991).
- [18] G. Bistoni, Finding chemical concepts in the hilbert space: Coupled cluster analyses of noncovalent interactions, *Wiley Interdisciplinary Reviews: Computational Molecular Science* **10**, e1442 (2020).
- [19] S.-J. Lv, P.-Y. Zhang, K.-L. Han, and G.-Z. He, Exact quantum scattering study of the Ne+H₂⁺ reaction on a new *ab initio* potential energy surface, *The Journal of Chemical Physics* **132**, 014303 (2010).
- [20] J. Xiao, C.-L. Yang, X.-F. Tong, M.-S. Wang, and X.-G. Ma, Quasi-classical trajectory study of the Ne+H₂⁺ → NeH⁺+H reaction based on global potential energy surface, *The Journal of Physical Chemistry A* **115**, 1486 (2011).
- [21] P. Siska, Molecular-beam studies of penning ionization, *Reviews of Modern Physics* **65**, 337 (1993).
- [22] A. B. Henson, S. Gersten, Y. Shagam, J. Narevicius, and E. Narevicius, Observation of resonances in penning ionization reactions at sub-kelvin temperatures in merged beams, *Science* **338**, 234 (2012).
- [23] S. Tanteri, S. D. S. Gordon, J. Zou, and A. Osterwalder, Study of He*/Ne*+Ar, Kr, N2, H2, D2 Chemi-Ionization Reactions by Electron Velocity-Map Imaging, *The Journal of Physical Chemistry A* **125**, 10021 (2021).
- [24] Y. Shagam, A. Klein, W. Skomorowski, R. Yun, V. Averbukh, C. P. Koch, and E. Narevicius., Molecular hydrogen interacts more strongly when rotationally excited at low temperatures leading to faster reactions, *Nature Chem.* **7**, 921 (2015).
- [25] A. Blech, Y. Shagam, N. Hölsch, P. Paliwal, W. Skomorowski, J. W. Rosenberg, N. Bibelnik, O. Heber, D. M. Reich, E. Narevicius, and C. P. Koch, Phase protection of Fano-Feshbach resonances, *Nature Commun.* **11**, 999 (2020).
- [26] Supplemental Material.
- [27] S. G. Johnson, The nlopt nonlinear-optimization package, <http://github.com/stevengj/nlopt>.
- [28] O. T. Unke and M. Meuwly, Toolkit for the construction of reproducing kernel-based representations of data: Application to multidimensional potential energy surfaces, *Journal of Chemical Information and Modeling* **57**, 1923 (2017).
- [29] H.-J. Werner, P. J. Knowles, F. R. Manby, J. A. Black, K. Doll, A. Heßelmann, D. Kats, A. Köhn, T. Korona, D. A. Kreplin, *et al.*, The Molpro quantum chemistry package, *The Journal of Chemical Physics* **152**, 144107 (2020).

SUPPLEMENTARY INFORMATION

A. Potential energy surfaces

The CCSD(T)-5 PES is a reproducing kernel Hilbert space²⁸ (RKHS) representation of CCSD(T)/aug-cc-pV5Z reference energies computed using MOLPRO²⁹ for a grid of Jacobi coordinates (R, r, θ) . Here, r is the H₂⁺ diatomic bond length, R is the distance between the center of mass of the diatomic molecule and the neon atom and θ is the angle between \vec{r} and \vec{R} . The grid (on-grid points) included 39 points for $r \in [1.1 a_0, 8.0 a_0]$, 49 points for $R \in [1.0 a_0, 45.0 a_0]$ and 10 Gauss-Legendre quadrature points for $\theta \in [0^\circ, 90^\circ]$.⁸ The root mean squared errors (RMSE) for energies of 250 geometries that were not used in constructing the RKHS representation (off-grid points) between reference calculations and the evaluated RKHS is 11.8 cm⁻¹, compared with an RMSE of 11.3 cm⁻¹ for on-grid points.⁸ This compares with RMSEs of 94 cm⁻¹ (0.27 kcal/mol) and 315 cm⁻¹ (0.0391 eV) for the MRCI-5 and MRCI-4 PESs, respectively.^{19,20}

Figure S1 shows a two dimensional slice in θ and R of the various potential energy surfaces at $r = 2.0 a_0$, which is near to the H₂⁺ equilibrium distance. At short range there is close agreement between CCSD(T)-5 and MRCI-5 for all angles θ , whilst MRCI-4 shows large deviations (both radially and angularly) from the other two that grow larger in the vicinity of the minimum around $R \approx 3.4 a_0$.

In contrast, Fig. S3 demonstrates the long range behaviour of the potential in terms of the Legendre expansion coefficients $V(R, r, \theta) = \sum_{\lambda=0}^{\infty} V_{\lambda}(R, r) P_{\lambda}(\cos \theta)$ at $r = 2.0 a_0$, which is near to the equilibrium distance of H₂⁺. We observe that as the interparticle distance R increases, the isotropic term $\lambda = 0$ of the CCSD(T)-5 potential energy surface shows a large deviation from both of the other potential energy surfaces.

B. Optimised scaling

Experimental noise leads to a certain portion of the cross section appearing where it should not (i.e., in between peaks, as can be seen for kinetic energies in the range of 200 cm⁻¹ and 500 cm⁻¹, for instance). As such, the scaling technique of Eq. (1) leads to a slight overestimation of the theoretical peak heights relative to the experimental ones (because a higher proportion of the overall area of the cross section curve is concentrated on the peaks). By simultaneously optimising for both the scale and the shift in energy according to

$$\begin{aligned} \Delta_{\text{opt}} &= \min_{b, E_{\text{shift}}} \Delta(b, E_{\text{shift}}) & (S1) \\ &= \min_{b, E_{\text{shift}}} \left(\int_{\mathbb{R}_+} dE_{\text{kin}} \right. \\ &\quad \left. \times |\sigma_{\text{exp}}(E_{\text{kin}}) - b\tilde{\sigma}_{\text{theory}}(E_{\text{kin}} + E_{\text{shift}})|^2 \right)^{-1/2}, \end{aligned}$$

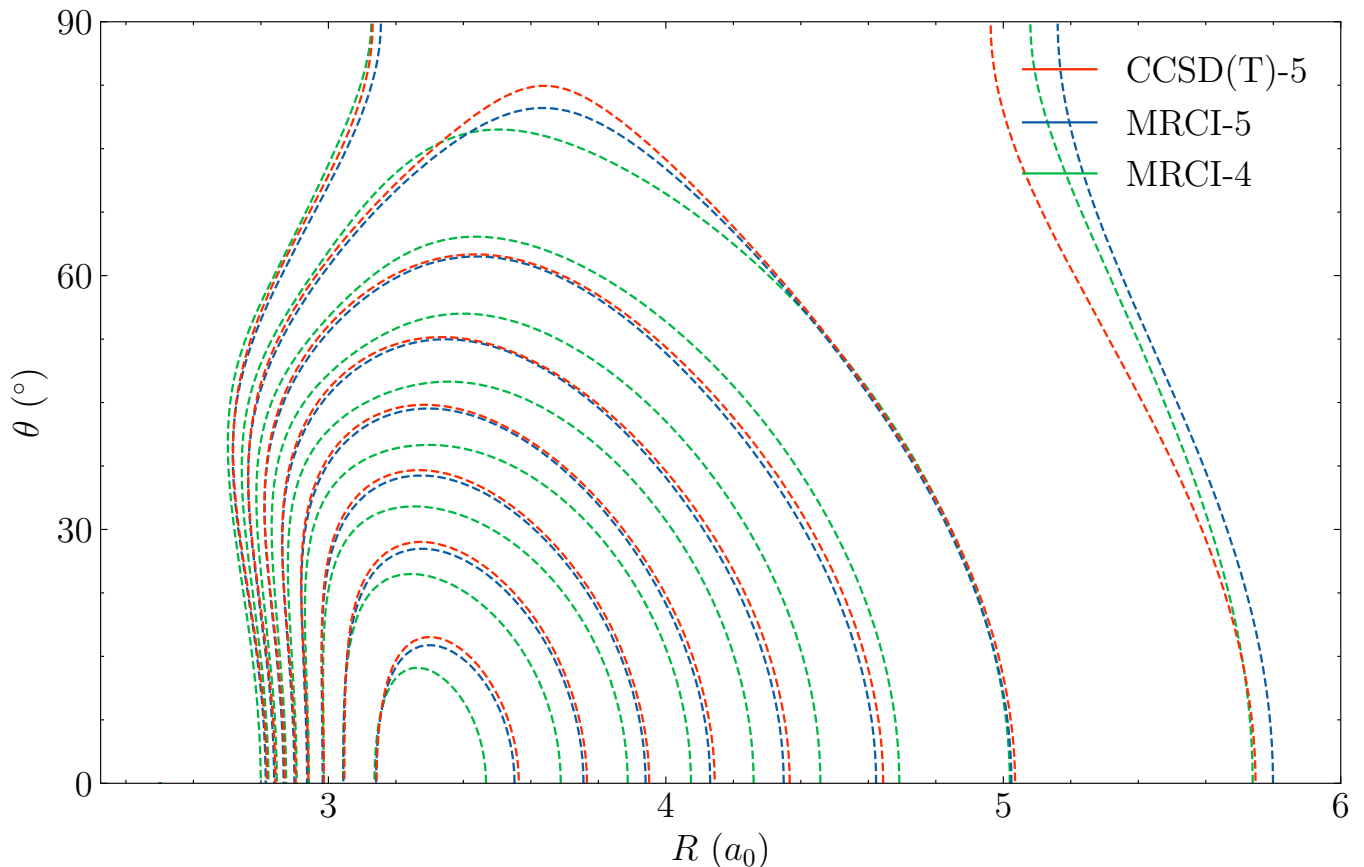


FIG. S1. Comparison of potential energy surfaces for a specific slice of coordinate space ($r = 2.0 a_0$) in the strongly interacting, bound state region. Each potential energy surface has the same set of contours (starting at -500 cm^{-1} around $R \approx 5.8 a_0$ and decreasing in steps of 500 cm^{-1} towards the minimum at $R \approx 3.3 a_0$ (note that the MRCI-4 surface has an additional contour corresponding to -4500 cm^{-1} , which is lower than the minimal energies of CCSD(T)-5 and MRCI-5 for the shown slice). The zero of energy was determined as the potential energy surface value at $r = 2.0 a_0$ and $R = 1000 a_0$.

we can find the best possible scale for the simulated cross section in the RMS deviation sense. Above, we have $a = 1/\int dE_{\text{kin}} \bar{\sigma}_{\text{exp}}(E_{\text{kin}})$ and the rescaled theoretical cross section is determined by the new, optimised parameter b .

The cross sections as a function of kinetic energy scaled with the optimised scaling parameter are shown in Figs. S4 and S5 for $v = 1$ and $v = 2$ respectively. At the cost of additional complexity, these reveal an overall better fit with the experimental cross section curve in terms of the various peak heights when compared to their ‘normalised’ counterparts. Conversely, the peaks in the simulated cross sections with ‘normalised scaling’ shown in Figs. 1 and 2 demonstrate a clear trend of overshadowing their measured counterparts, mostly notably for the $j' = 3, 5$ and 7 peaks in the case of the CCSD(T)-5 and MRCI-5 PES. Table S2 shows the difference that the chosen scaling scheme makes in terms of the figure of merit \mathcal{F} , (energy-shifted) RMS deviation $\min_{E_{\text{shift}}} \Delta(E_{\text{shift}})$ and optimal energy shift $E_{\text{shift}}^{(\text{opt})}$. Significantly, for $v = 2$, it is seen that in the optimised scaling scheme, the CCSD(T)-5 PES outperforms the

MRCI-4 PES when it comes to $\min_{E_{\text{shift}}} \Delta(E_{\text{shift}})$. In contrast, when using the scaling of Eq. (1), the energy shifted RMS deviation $\min_{E_{\text{shift}}} \Delta(E_{\text{shift}})$ for $v = 2$ was minimal for the MRCI-4 PES. In this case the most notable difference is in the overestimation of the height of the peak comprised of the $v' = 1$ and $j' = 2, 3$ as well as the $v' = 0$ and $j' = 9$ final states, as well as the peak due to $v' = 1$ and $j' = 7$ for the CCSD(T)-5 PES. It is seen that optimised rescaling causes the energy shifted RMS deviation to drop by $1.8 \cdot 10^{-3}$ in the case of CCSD(T)-5, whilst the improvement for the MRCI-4 PES is more moderate at $0.3 \cdot 10^{-3}$. The figure of merit \mathcal{F} is affected in a similar way, with a larger margin of improvement observed for CCSD(T)-5, causing it to more clearly outperform the other PES when utilising optimised scaling.

C. Regularisation

We have accounted for the presence of noise in the experimental cross section by investigating whether a regularisation technique, similar to that employed in¹⁶,

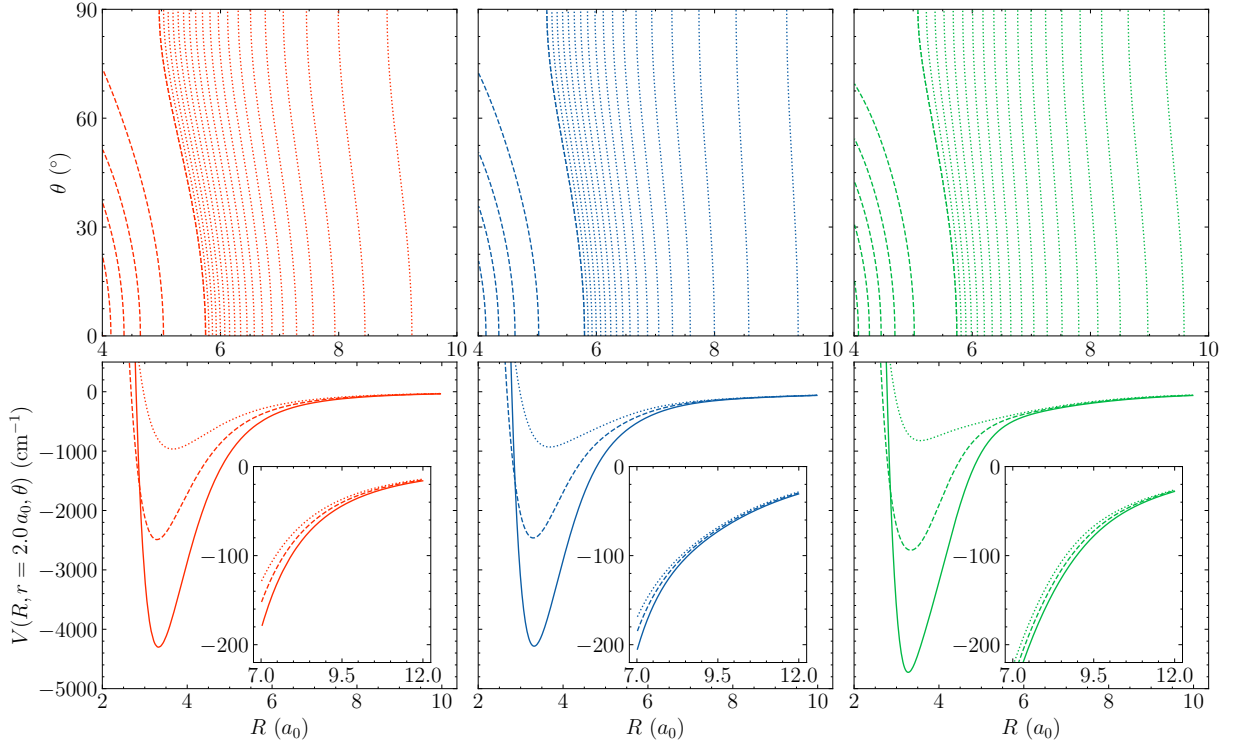


FIG. S2. Comparison of PESs focusing on the long-range part. Top panels from left to right: PESs CCSD(T)-5 , MRCI-5 and MRCI-4 for $R \in [4, 10] a_0$ and $r = 2.0 a_0$. With increasing R the anisotropy for MRCI-5 reduces considerably compared with the other two PESs. Spacing between dashed line contours is 500 cm^{-1} as before whilst the spacing between dotted contours is 25 cm^{-1} . Bottom panels: selected one dimensional cuts for $\theta = 0^\circ$ (solid), 45° (dashed) and 90° (dotted lines), with $r = 2.0 a_0$. Inset panels show a close up of the long range behaviour, emphasising the differences in both spread and anisotropy even at large R . As above, the CCSD(T)-5 , MRCI-5 and MRCI-4 contours and graphs are shown in red, blue and green respectively.

influences the results. Regularisation was implemented by subtracting δ_{reg} from the difference in cross sections, whilst ensuring the kinetic energy-dependent difference never drops below zero

$$\epsilon(E_{\text{kin}}) = \max(|\sigma_{\text{exp}}(E_{\text{kin}}) - \sigma_{\text{shift}}(E_{\text{kin}})| - \delta_{\text{reg}}, 0), \quad (\text{S2})$$

where $\sigma_{\text{shift}}(E_{\text{kin}})$ is the shifted and rescaled simulated cross section under either scaling method. The non-

regularised difference between cross sections in the expressions for $\Delta(E_{\text{shift}})$ can then be replaced with the regularised expression $\Delta_{\text{reg}}(E_{\text{shift}})$. Whilst it was observed that regularisation does indeed affect the RMS deviation and figure of merit (whose regularised counterpart is denoted by \mathcal{F}_{reg}) as summarised in Table S2, the cross sections due to all PES are affected in almost the same way, i.e., regularisation does not qualitatively impact the PES comparison results.

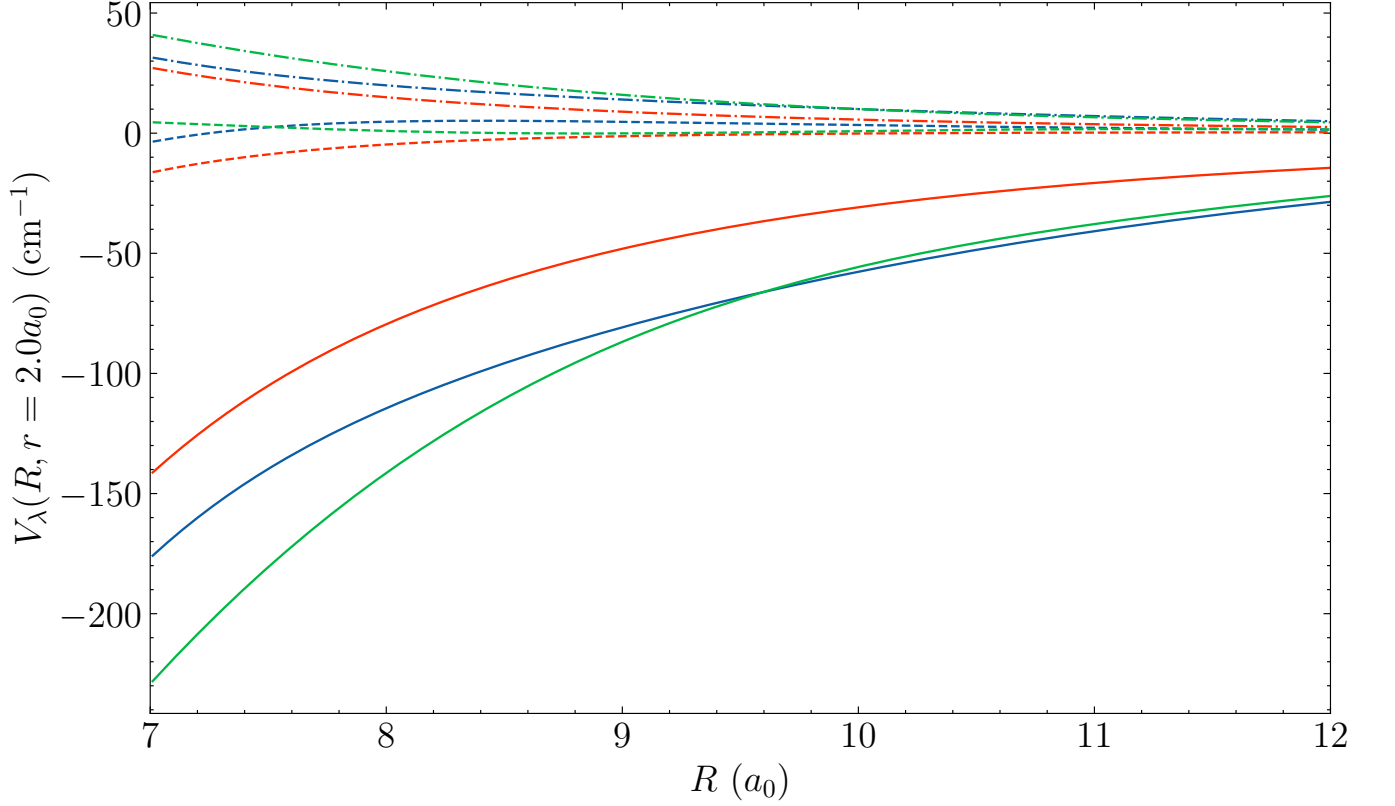


FIG. S3. Comparison of the long range behaviour of the various potential energy surfaces, portrayed in terms of the R -dependent Legendre coefficients $V_\lambda(R, r)$ for a fixed equilibrium distance $r = 2 a_0$. Large deviations are seen between the isotropic $\lambda = 0$ curve for CCSD(T)-5 and those corresponding to the other two potential energy surfaces. The solid, dashed and dash-dotted lines correspond to $\lambda = 0, 2$ and 4 respectively.

v	scaling	PES	\mathcal{F}	\mathcal{F}_{reg}	$\min_{E_{\text{shift}}} \Delta(E_{\text{shift}})$	$\min_{E_{\text{shift}}} \Delta_{\text{reg}}(E_{\text{shift}})$	$E_{\text{shift}}^{(\text{opt})}$
1	Eq. (1)	CCSD(T)-5	$9.9 \cdot 10^{-3}$	$8.0 \cdot 10^{-3}$	$9.9 \cdot 10^{-3}$	$8.0 \cdot 10^{-3}$	-0.74cm^{-1}
		MRCI-5	$1.2 \cdot 10^{-2}$	$1.0 \cdot 10^{-2}$	$1.0 \cdot 10^{-2}$	$8.1 \cdot 10^{-3}$	21.0cm^{-1}
		MRCI-4	$1.1 \cdot 10^{-2}$	$9.4 \cdot 10^{-3}$	$7.9 \cdot 10^{-3}$	$6.0 \cdot 10^{-3}$	30.0cm^{-1}
	Eq. (S1)	CCSD(T)-5	$7.4 \cdot 10^{-3}$	$5.1 \cdot 10^{-3}$	$7.4 \cdot 10^{-3}$	$5.1 \cdot 10^{-3}$	-0.86cm^{-1}
		MRCI-5	$1.0 \cdot 10^{-2}$	$8.0 \cdot 10^{-3}$	$8.1 \cdot 10^{-3}$	$5.8 \cdot 10^{-3}$	21.0cm^{-1}
		MRCI-4	$9.9 \cdot 10^{-3}$	$8.0 \cdot 10^{-3}$	$6.6 \cdot 10^{-3}$	$4.5 \cdot 10^{-3}$	29.0cm^{-1}
2	Eq. (1)	CCSD(T)-5	$8.5 \cdot 10^{-3}$	$7.0 \cdot 10^{-3}$	$8.5 \cdot 10^{-3}$	$7.0 \cdot 10^{-3}$	-0.54cm^{-1}
		MRCI-5	$1.1 \cdot 10^{-2}$	$9.1 \cdot 10^{-3}$	$9.7 \cdot 10^{-3}$	$8.3 \cdot 10^{-3}$	16.0cm^{-1}
		MRCI-4	$9.0 \cdot 10^{-3}$	$7.6 \cdot 10^{-3}$	$7.3 \cdot 10^{-3}$	$6.1 \cdot 10^{-3}$	27.0cm^{-1}
	Eq. (S1)	CCSD(T)-5	$6.7 \cdot 10^{-3}$	$5.0 \cdot 10^{-3}$	$6.7 \cdot 10^{-3}$	$5.0 \cdot 10^{-3}$	-0.68cm^{-1}
		MRCI-5	$7.8 \cdot 10^{-3}$	$6.1 \cdot 10^{-3}$	$6.9 \cdot 10^{-3}$	$5.1 \cdot 10^{-3}$	16.0cm^{-1}
		MRCI-4	$8.6 \cdot 10^{-3}$	$7.2 \cdot 10^{-3}$	$7.0 \cdot 10^{-3}$	$5.7 \cdot 10^{-3}$	27.0cm^{-1}

TABLE S2. Expanded version of Table I, including regularisation and the alternative cross section scaling scheme introduced in Eq. (S1). For both “initial” vibrational states, the PES that performs best for a given quantifier is highlighted, using the color code of Figs. 1 and 2.

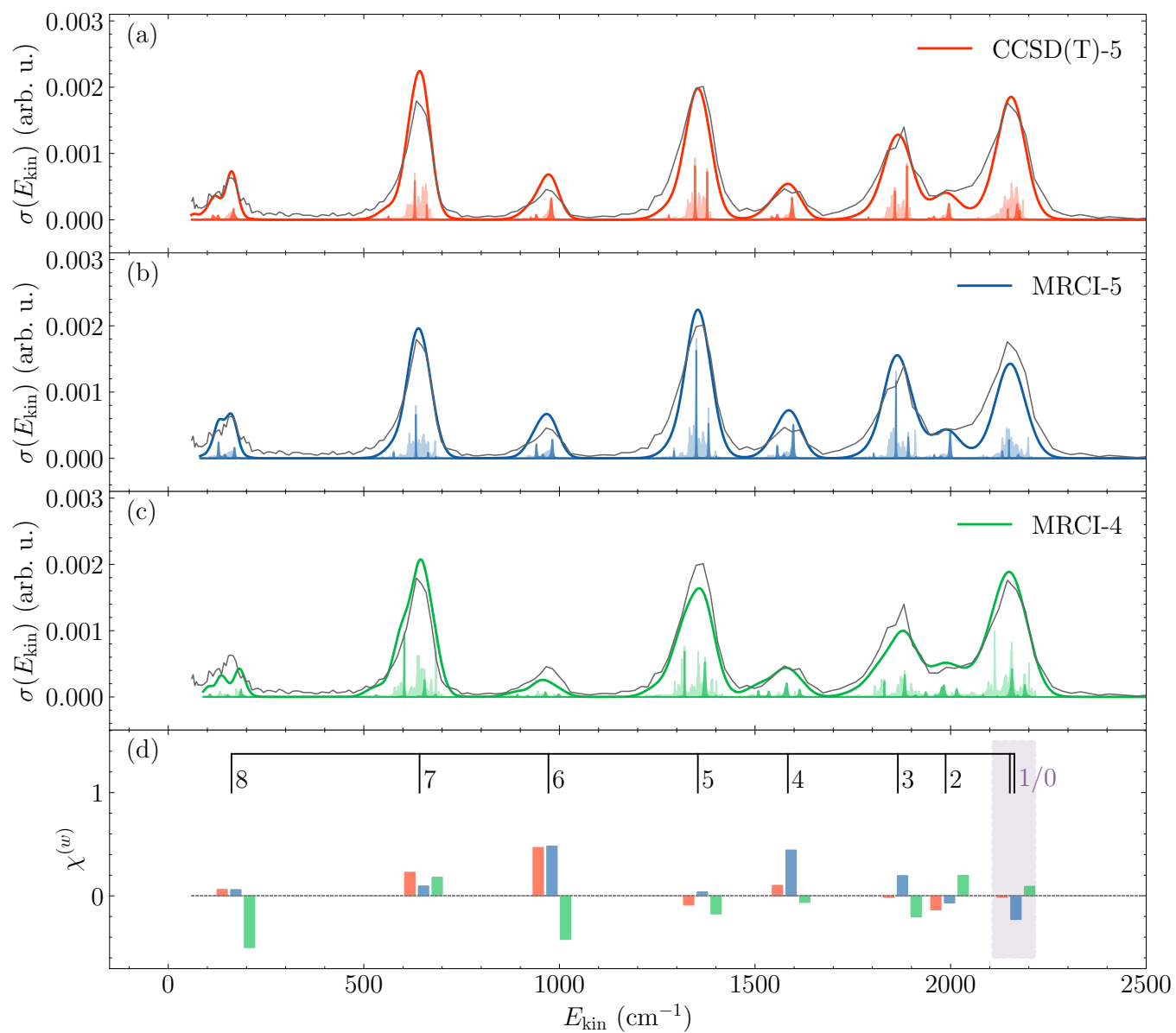


FIG. S4. Same as Fig. 1, but with the fitted relative scaling of Eq. (S1).

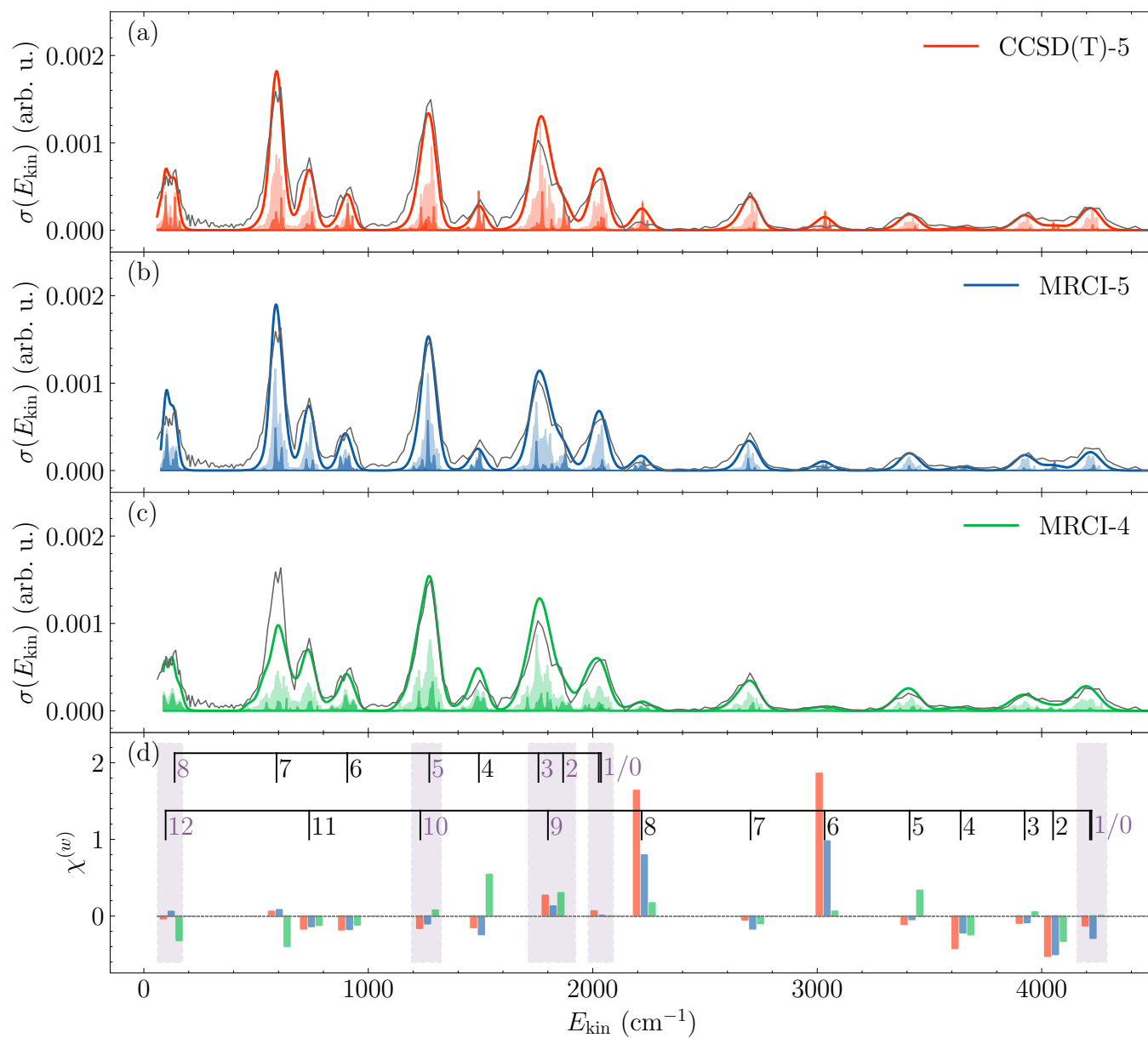


FIG. S5. Same as Fig. 2, but with the fitted relative scaling of Eq. (S1).